Dalton Transactions

ROYAL SOCIETY OF CHEMISTRY

PAPER

View Article Online
View Journal | View Issue

Cite this: *Dalton Trans.*, 2025, **54**, 10254

Amorphous Ni–Fe–B bimetallic borides: boron-mediated synergy for ultrafast and stable 4-nitrophenol reduction†

Jianquan Wang,‡[a] Fangzheng Qi,‡[a] Dong Ma,[a] Guang-Ning Liu *[a] and Cuncheng Li *[a,b]

Received 12th April 2025,
Accepted 2nd June 2025

DOI: 10.1039/d5dt00871a

rsc.li/dalton

The efficient reduction of 4-nitrophenol (4-NP) to 4-aminophenol (4-AP) has garnered significant interest in the fields of environmental remediation and chemical manufacturing. However, conventional catalytic reduction methods encounter challenges such as insufficient catalyst activity, poor stability, and high costs. Nickel–iron bimetallic systems offer promise due to their synergistic effects, and recent studies have shown that boron incorporation (Ni–Fe–B) further enhances activity through electronic modulation and improved charge transfer. Despite these advantages, the potential of Ni–Fe–B for 4-NP reduction remains largely unexplored. In this study, a series of Ni–Fe–B catalysts with tunable Ni/Fe ratios were synthesized *via* ultrasound-assisted reduction and evaluated for the catalytic reduction of 4-NP at room temperature. By systematically adjusting the Ni/Fe molar ratio, we optimized the morphology and electronic structure of the catalysts, leading to significantly enhanced catalytic performance. Notably, this study pioneers the application of Ni–Fe–B catalysts for 4-NP reduction. Remarkably, the Ni_3Fe_1–B sample demonstrated exceptional activity, achieving complete 4-NP conversion within just 3 minutes, surpassing the performance of monometallic borides (Ni–B or Fe–B). This enhancement is attributed to the strong synergistic effect between Ni and Fe, where electron redistribution facilitated by boron incorporation promotes hydrogenation kinetics. Furthermore, Ni_3Fe_1–B exhibited excellent cycling stability, maintaining high activity over multiple runs without significant degradation, which is crucial for practical applications. These findings not only establish Ni–Fe–B as a highly efficient catalyst system for 4-NP reduction but also provide fundamental insights into the design of bimetallic boride materials for sustainable chemical transformations.

Introduction

Nitroaromatic compounds are widely utilized in the chemical industry as raw materials for pesticides, explosives and other chemical products, contributing significantly to environmental pollution, particularly water pollution, and thereby posing a threat to living organisms.[1–5] 4-Nitrophenol (4-NP) is a highly toxic nitroaromatic compound that resists degradation in natural environments and can bioaccumulate over time. It is classified as carcinogenic, hepatotoxic, and mutagenic, presenting significant risks to human health.[6–8] Various methods have been employed to mitigate the hazards associated with 4-NP, including electrochemical treatment,[9] Fenton degradation,[10–12] photocatalytic degradation,[13,14] microbial degradation,[15,16] microwave catalytic oxidation,[17] adsorption,[18–20] and electrocatalytic reduction.[21–25] However, these methods are often complicated and costly, leading to growing interest in the green and straightforward reduction of 4-NP to 4-aminophenol (4-AP) using sodium borohydride ($NaBH_4$) as a reducing agent. This approach is advantageous as it operates under mild conditions and can be performed in aqueous media. Furthermore, 4-AP is an important compound that finds widespread application in dyes, pharmaceuticals, and pesticides.[26–29] Despite its potential, the slow self-hydrolysis of $NaBH_4$ significantly hampers the rate of hydrogenation, making the presence of a catalyst essential for efficient reactions.[30] Therefore, developing cost-effective catalysts with high catalytic activity is of paramount importance.

So far, a considerable number of catalysts have been developed for the catalytic reduction of nitroaromatic compounds.[31,32] Significantly, noble metal-based catalysts

[a]*School of Chemistry and Chemical Engineering, University of Jinan, Jinan 250022, P. R. China. E-mail: chm_liugn@ujn.edu.cn, chm_licc@ujn.edu.cn*
[b]*Collaborative Innovation Center of Yellow River Basin Pharmaceutical Green Manufacturing and Engineering Equipment, University of Jinan, Jinan 250022, P. R. China*

†Electronic supplementary information (ESI) available. See DOI: https://doi.org/10.1039/d5dt00871a

‡These authors contributed equally to this work.

have been extensively studied due to their high catalytic efficiency in the hydrogenation of 4-NP to 4-AP.[33–35] However, their widespread application is constrained by issues of scarcity and high costs. Consequently, there is a pressing need for more accessible and economical alternatives, such as non-precious transition metal borides, nitrides, carbides, sulfides, selenides, and phosphides.[36–39] Transition metal-based borides, in particular, have garnered significant attention for their low cost and potential catalytic activity.[40–42] More metal borides can be obtained by ultrafast synthesis, which exhibit good catalytic performance.[43–45] Previous research indicates that NiB_2 exhibits superior catalytic properties compared to pure nickel catalysts.[46] However, metal borides tend to aggregate into larger particles during synthesis,[47] which diminishes their catalytic activity. The introduction of another metal element can effectively inhibit the aggregation of catalyst particles and adjust the adsorption of reactants on the active sites, thus affecting the catalytic activity.[48] For instance, Ni-supported Co–Mo–B catalysts have demonstrated promising catalytic capabilities for the hydrolysis of $NaBH_4$.[49,50] Furthermore, the optimized ratio of Ni/Fe/B in the NiFeB catalyst can provide abundant synergistic active sites for the N_2 reduction reaction,[51] and the intervention of Fe is helpful for the formation of electron-rich metal centers and strong acidic centers within the catalyst.[52] These examples encourage us to construct efficient bimetallic borides for catalytic reduction of 4-NP to 4-AP.

In this work, we developed amorphous nickel–iron bimetallic boride (Ni–Fe–B) catalysts *via* a facile ultrasound-assisted reduction method for efficient 4-NP reduction at ambient temperature. Remarkably, the optimized Ni_3Fe_1–B catalyst achieved >99% conversion of 400 mg L^{-1} 4-NP (80 mL) within 3 minutes, exhibiting an outstanding apparent rate constant (1.363 min^{-1}). Systematic comparisons revealed that both boron incorporation and Ni–Fe synergy are critical: (i) boron modulates the electronic structure, enhancing electron transfer from BH_4^- to 4-NP, while (ii) the bimetallic interaction optimizes intermediate adsorption. Furthermore, Ni_3Fe_1–B demonstrated excellent cycling stability over ten consecutive runs with negligible activity loss (<10%), underscoring its practical potential for wastewater treatment. To our knowledge, this work represents the first demonstration of Ni–Fe–B as a catalyst for 4-NP reduction.

Experimental section

Chemicals and materials

All materials were used as received without additional purification. Nickel(II) nitrate hexahydrate ($Ni(NO_3)_2{\cdot}6H_2O$, 99.9%) and iron(III) nitrate nonahydrate ($Fe(NO_3)_3{\cdot}9H_2O$, 99%) were obtained from Sigma-Aldrich. Sodium borohydride ($NaBH_4$, 98%), anhydrous ethanol (EtOH, 99.7%) and 4-nitrophenol (4-NP, 99%) were sourced from Sinopharm Chemical Reagent Co. Ltd. Ultrapure water (Millipore, 18.25 MΩ cm^{-1}) was used in all experiments.

Synthesis of Ni_3Fe_1–B

Bimetallic Ni_3Fe_1–B was synthesized through ultrasound-assisted reduction. Initially, 0.6 mmol of $Ni(NO_3)_2{\cdot}6H_2O$ and 0.2 mmol of $Fe(NO_3)_3{\cdot}9H_2O$ were dissolved in 5 mL of absolute ethanol and sonicated for 5 minutes to form a metal salt solution. Subsequently, 1.0 mL of freshly prepared $NaBH_4$ (1.6 mol L^{-1}) was added dropwise to the metal salt solution, resulting in immediate formation of bubbles and black precipitates. Sonication was continued for 30 minutes until no more bubbles were observed, indicating complete reduction of Ni^{2+} and Fe^{3+}. The black precipitate was then centrifuged, washed multiple times with absolute ethanol, and finally dried in a vacuum oven at 40 °C for 12 hours to obtain the Ni_3Fe_1–B samples.

Bimetallic Ni–Fe borides were synthesized using a similar method for comparison purposes. The total metal content in the metal salt solution was maintained at 0.8 mmol. The Ni/Fe molar ratios in the initial metal salt solution were varied to 3 : 1, 1 : 1, and 1 : 3, resulting in the production of Ni_3Fe_1–B, Ni_1Fe_1–B, and Ni_1Fe_3–B, respectively. These names are based on the actual metal molar ratios determined by subsequent ICP-OES analysis of bimetallic borides.

Catalyst characterization

The morphological and structural characteristics of the synthesized samples were studied in detail using various analytical techniques. Field emission scanning electron microscopy (FESEM, Gemini300), transmission electron microscopy (TEM, JEM-1400) and high-resolution transmission electron microscopy (HRTEM, JEM-2100F) were used to observe the morphology of the samples. Elemental profiling of samples was performed by means of a built-in energy dispersive spectrometer (EDS). X-ray diffraction (XRD) spectra were obtained using a Bruker D8 Focus 2000 X-ray diffractometer and X-ray photoelectron spectroscopy (XPS) analysis was performed with a Thermal Science ESCALAB 250XI system. The actual metal molar ratios of the samples were determined using inductively coupled plasma mass spectrometry (ICP-OES, ICAP-7200). The specific surface area of the sample was measured *via* nitrogen adsorption desorption isotherm measurement using a specific surface area and pore size analyzer (BET, Tristar II 3020). In addition, monitoring of catalytic reaction changes was performed using an ultraviolet-visible absorption spectrophotometer (UV-vis, UV-1900).

Testing the catalytic performance

The reduction of 4-NP by $NaBH_4$ served as a model reaction to test the catalytic activity of the prepared samples. The reaction was typically carried out in a beaker at room temperature, and monitored using UV-vis spectroscopy. An aqueous solution of 4-NP (80 mL, 400 mg L^{-1}) was mixed with 2 mL of $NaBH_4$ (1.0 mol L^{-1}) to form a bright yellow solution. Subsequently, Ni_3Fe_1–B dispersed in absolute ethanol (0.5 mL, 10 mg mL^{-1}) was added to the yellow reaction solution described above. During the reaction, 150 μL of the reaction supernatant was collected, diluted to 3 mL with ultrapure water, and tested

using a UV-vis absorption spectrophotometer with a scanning range of 250–500 nm. The apparent rate constant (k_{app}) was calculated using the following equation (eqn (1)):

$$-k_{app} \cdot t = \ln\left(\frac{C_t}{C_0}\right) = \ln\left(\frac{A_t}{A_0}\right) \quad (1)$$

where C_t and C_0 represent the concentrations of 4-NP at time t and the initial state. The concentration (C) is directly proportional to the absorbance (A) according to Beer's law.

In the cycling test, ten consecutive reactions of Ni_3Fe_1–B were measured. After the first run, 75 mg of $NaBH_4$ and 1.0 mL of 32 g L^{-1} 4-NP were added directly to the reaction system for the second run, and the same process occurred for the next runs.

Results and discussion

Preparation and structural characterization of Ni_3Fe_1–B

Ni–Fe–B catalysts were synthesized by a one-step process as shown in Fig. 1a. In the reaction, $NaBH_4$ not only acts as a strong reductant, but also acts as a boron source, releasing a large amount of boron, which is integrated into the metal matrix, thus promoting the formation of metal borides.[53]

As indicated in Tables S1 and S3,† the ICP-OES and XPS elemental analysis confirmed the successful synthesis of Ni–Fe–B catalysts with varying Ni/Fe metal ratios. The XRD diffraction pattern shown in Fig. 1b shows no distinct diffraction peaks, indicating that Ni_3Fe_1–B has an amorphous structure. Meanwhile, Fig. S1† shows that Ni–Fe–B catalysts with different metal ratios all exhibit an amorphous structure, aligning with previous studies.[54] Further TEM morphological studies revealed that Ni_3Fe_1–B is composed mainly of irregular nanosheets (Fig. 1c–e). From Fig. S2a,† it is observed that Ni–B has obvious aggregation of nanosheets, but it is improved in Ni_3Fe_1–B. These results indicate that proper Fe addition affects the aggregation process of the catalyst, but excessive Fe addition makes the nanosheets broken (Fig. S2b–d†). Nanoflowers formed by stacking of nanosheets can be detected in FESEM images of Ni_3Fe_1–B (Fig. S3†), which is consistent with TEM results. Importantly, no dots or distinct rings were found in the selected area electron diffraction (SAED) pattern

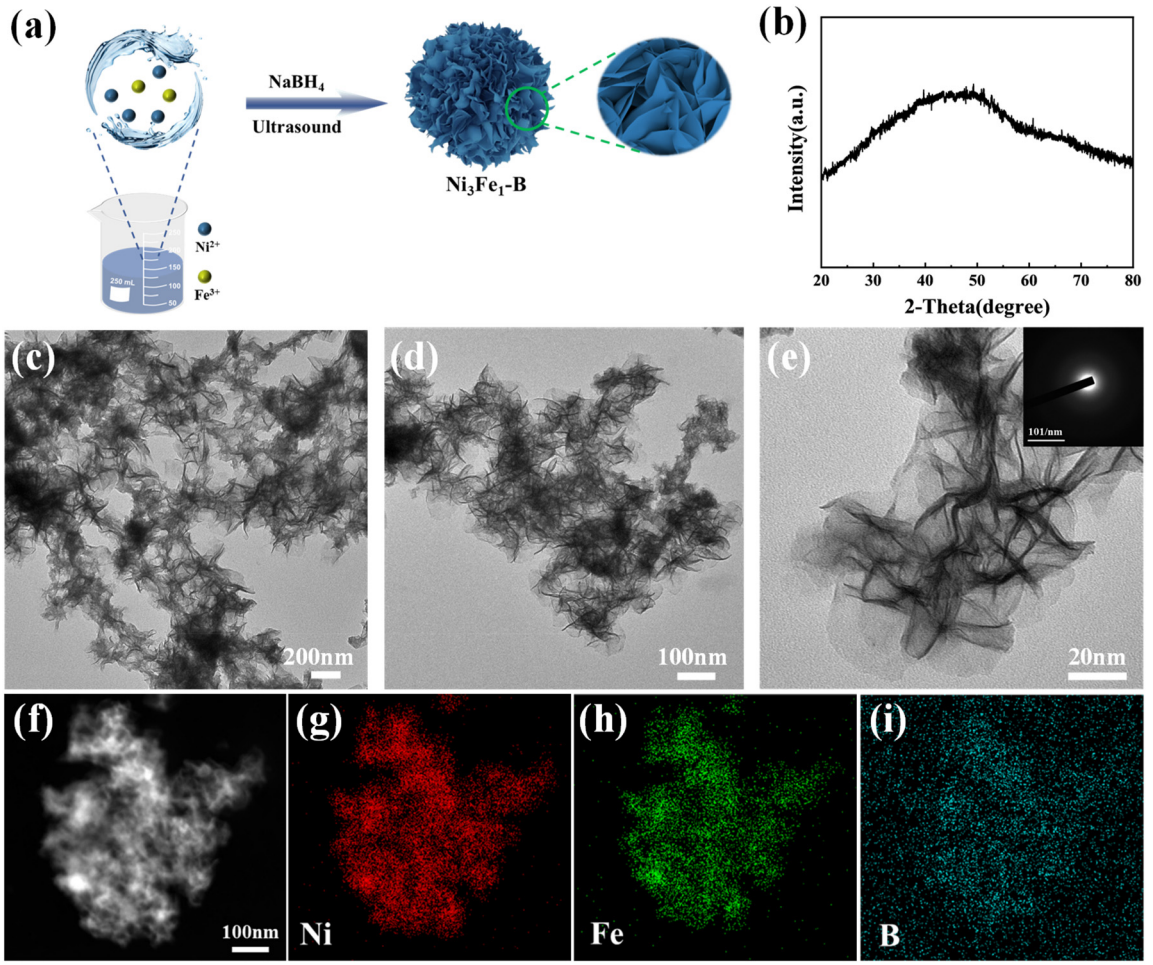

Fig. 1 (a) Schematic diagram of the synthesis of Ni_3Fe_1–B; (b) XRD patterns of Ni_3Fe_1–B; (c and d) TEM images and (e) HRTEM image of Ni_3Fe_1–B (inset: SAED pattern of the sample); and (f–i) elemental mapping of Ni, Fe and B.

of Ni_3Fe_1–B (inset in Fig. 1e), further confirming the amorphous structure of Ni_3Fe_1–B. In addition, elemental mapping of the Ni_3Fe_1–B sample shows that Ni, Fe and B elements are uniformly distributed on the catalyst surface, indicating the successful formation of Ni–Fe–B catalysts (Fig. 1f–i).

The surface chemical state and electronic structure of Ni_3Fe_1–B were further analyzed using XPS. Fig. 2 shows XPS spectra of (a) survey, (b) Ni 2p, (c) Fe 2p and (d) B 1s. The whole scanning survey spectrum indicates the existence of Ni, Fe and B (Fig. 2a), which is consistent with the EDS analysis (Fig. S4†). All elements were calibrated with a C 1s peak at 284.8 eV. As shown in Fig. 2b, peaks from the Ni $2p_{3/2}$ spectrum correspond to Ni bonded to B (Ni–B, 852.5 eV), Ni^{2+} (856.2 eV and 873.7 eV) for nickel oxide/hydroxide, and satellite peaks, respectively.[55–57] The fitted peaks in the Fe $2p_{3/2}$ spectrum correspond to Fe bonded to B (Fe–B, 708.1 eV), Fe^{3+} and Fe^{2+} (712.4 eV, 715.6 eV and 725.8 eV).[58] The coexistence of metal and metal oxide species is thought to facilitate hydrogen activation and provide active sites for catalytic reactions.[56] For the B 1s spectrum (Fig. 2d), the peak at 192.1 eV confirms the presence of boron oxide species, while the peak at 187.8 eV indicates the formation of metal–boron bonds.[59,60] Boron oxide can accelerate the hydrolysis of BH_4^- to produce active hydrogen species (H*) through surface hydroxyl groups (–OH) and transfer them to nearby Ni/Fe active sites.

Catalytic reduction of 4-NP

The catalytic process was elucidated through the model reaction of 4-NP reduction to 4-AP. As shown in Fig. 3a, the original solution of 4-NP shows a distinct absorption peak at 317 nm, which shifts to 400 nm when freshly prepared $NaBH_4$ is added, due to deprotonation under alkaline conditions. After adding only $NaBH_4$ to the 4-NP solution and letting it stand for 30 minutes, no spectral changes were observed (Fig. 3b), indicating that catalytic hydrogenation does not occur even with an excess of $NaBH_4$ in the absence of a catalyst,[61,62] further demonstrating the importance of the catalyst. To demonstrate the essential role of a reducing agent, we conducted a control experiment in the absence of the reducing agent ($NaBH_4$). When only the catalyst was added to the 4-NP solution, the characteristic absorption peak decreased by merely 10% within 10 minutes (Fig. S5†), confirming that both the catalyst and reducing agent are indispensable for efficient 4-NP reduction. These results also indicate that there is only limited physical adsorption between the catalyst and reactants, and the rapid decrease of the 4-NP concentration during catalytic reduction is mainly due to catalytic reaction on active sites rather than the adsorption effect.

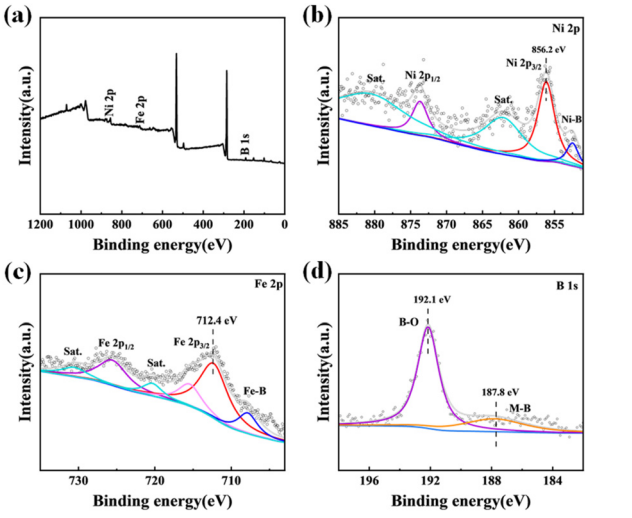

Fig. 2 The XPS spectra of (a) survey, (b) Ni 2p, (c) Fe 2p, and (d) B 1s of Ni_3Fe_1–B.

As shown in Fig. 3c, Ni_3Fe_1–B exhibits the highest catalytic efficiency, achieving complete conversion of 4-NP to 4-AP within just 3 minutes. Comparative studies reveal progressively slower reaction kinetics for other compositions: Ni–B (4 min, Fig. S6a†), Ni_1Fe_1–B (5 min, Fig. S6b†), Ni_1Fe_3–B (15 min, Fig. S6c†), and Fe–B (13 min for only ≈40% conversion, Fig. S6d†). The catalytic performance follows the order: Ni_3Fe_1–B > Ni–B > Ni_1Fe_1–B > Ni_1Fe_3–B > Fe–B (Fig. 3d), with Ni_3Fe_1–B demonstrating superior activity. Kinetic analysis based on pseudo-first-order reaction models further confirms this trend.[63–65] The linear plots of $\ln(A/A_0)$ *versus* time (Fig. 3e and f) yield apparent rate constants (k_{app}) of 1.363 min^{-1} (Ni_3Fe_1–B), 1.118 min^{-1} (Ni–B), 0.803 min^{-1} (Ni_1Fe_1–B), 0.198 min^{-1} (Ni_1Fe_3–B), and 0.014 min^{-1} (Fe–B). The steepest slope and highest k_{app} value observed for Ni_3Fe_1–B indicate its optimal charge transfer kinetics. These results unambiguously demonstrate that: (1) Ni–Fe bimetallic borides outperform their monometallic counterparts, and (2) the Ni/Fe atomic ratio critically determines catalytic performance through synergistic electronic effects.

To elucidate the role of boron incorporation and reducing agent selection, we systematically evaluated the catalytic performance under different conditions. First, comparative studies between Ni_3Fe_1–B and NiFe alloy revealed that boron doping significantly enhances catalytic activity by optimizing the electronic structure (Fig. S7a†). Second, when comparing different reducing agents, while $N_2H_4{\cdot}H_2O$ achieved similar conversion times, the apparent rate constant (k_{app}) was higher with $NaBH_4$ as the hydrogen source (Fig. S7b–d†), indicating its superior reduction capability in this system.

Table S2† shows a comparative analysis of the catalytic performance of the synthesized catalysts in this study and various nanomaterials from the existing literature for the reduction of 4-NP. It is noteworthy that Ni_3Fe_1–B exhibits catalytic activity superior to that of several noble metal-based catalysts. This remarkable activity of Ni_3Fe_1–B is attributed to the synergistic effect between nickel and iron, along with the electronic interaction between boron and metallic components, as confirmed by the previous analysis. Therefore, Ni_3Fe_1–B is the most efficient catalyst among the five materials synthesized in this study.

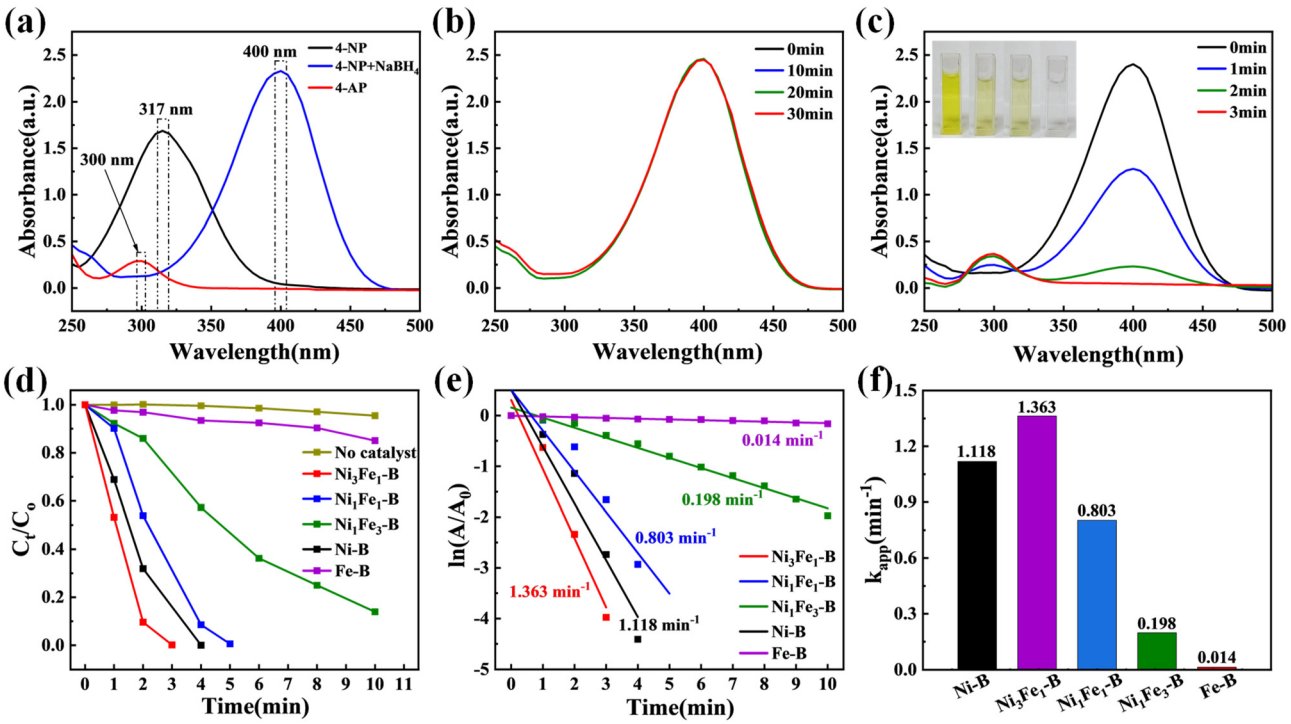

Fig. 3 (a) The UV-vis absorption spectra of 4-NP, 4-AP and 4-NP + $NaBH_4$; (b) UV-vis absorption spectrum of 4-NP reduction in the absence of a catalyst; (c) UV-vis absorption spectrum of Ni_3Fe_1–B; (d) plots of C_t/C_0 against the reaction time; (e) plots of $\ln(A/A_0)$ against the reaction time; and (f) the calculated k_{app} value in different catalysts.

Exploration of experimental conditions

The results show that there is a relationship between the catalytic rate on the catalyst surface and the initial concentration of 4-NP and the concentration of the reductant. The mechanism of 4-NP reduction was elucidated by varying the concentrations of (i) 4-NP (400–1000 mg L^{-1}) and (ii) $NaBH_4$ (0.33–1.32 mol L^{-1}). As shown in Fig. 4a–c and Fig. S8,† the reaction rate decreases with increasing 4-NP concentration, resulting in a corresponding decrease in k_{app} values. This is due to high concentrations of 4-NP and its reaction intermediates being readily adsorbed on the catalyst surface, which hinders desorption and inhibits catalytic reduction. Conversely, as shown in Fig. 4d–f and Fig. S9,† the reaction rate increases with increasing $NaBH_4$ concentration in the range of 0.33–1.0 mol L^{-1}. However, when the concentration increased to 1.32 mol L^{-1}, the reaction rate decreased slightly. This result indicates that excess reductant leads to competitive adsorption on the catalyst surface, thereby preventing 4-NP molecules from binding to the active site. This competition limits the availability of the active site of 4-NP, reducing overall conversion.

Stability evaluation

Catalyst stability is crucial for evaluating performance and practical applications. We evaluated the stability of Ni_3Fe_1–B through ten consecutive experiments at room temperature. As shown in Fig. 5a, the cycle test indicated that Ni_3Fe_1–B had excellent cycling performance over ten cycles. The catalytic performance of the catalyst slightly decreased after ten cycles but still maintained over 90%, as shown in Fig. S10.† Fig. 5b also shows that the absorbance value at 300 nm increased steadily during the reaction, along with the gradual accumulation of product 4-AP. Additionally, the XRD pattern (Fig. 5c) and TEM image (Fig. 5d) remained largely unchanged compared to the original catalyst, further confirming the excellent stability of Ni_3Fe_1–B in the catalytic reduction of 4-NP.

Catalytic reduction mechanism

Previous studies provide theoretical support for the catalytic reduction of 4-NP by Ni–Fe–B catalysts through density functional theory (DFT) calculations. First, studies on amorphous NiB_2 [46] reveal that boron facilitates electron transfer and substrate adsorption, analogous to 4-NP activation on Ni–Fe–B. Second, Co_xB research[66] shows that Ni/Fe ratios tune catalytic activity by modulating surface charge distribution. Third, boron-doped Ni/Fe nanohybrids[67] demonstrate bimetallic synergy and electron delocalization enhance hydrogenation. These findings align with the role of Ni_3Fe_1–B in adsorbing reactants and mediating electron transfer from BH_4^-.

Ni_3Fe_1–B nanostructures provide adsorption sites for reactants and facilitates electron transfer between BH_4^- (as an electron donor) and the nitro group (–NO_2, as an electron acceptor). Experimental results and the related literature indicate that the catalytic reduction process involves several key steps (Fig. 6): (I) adsorption of 4-NP and $NaBH_4$ on the Ni_3Fe_1–B

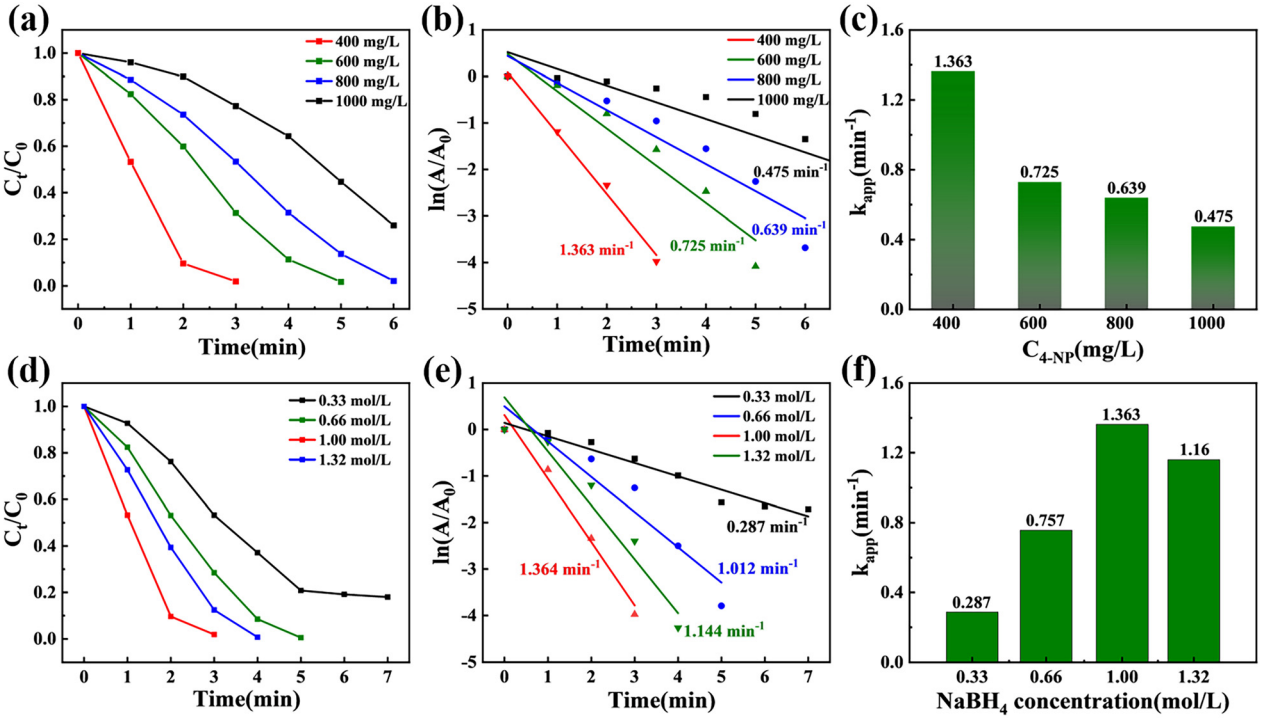

Fig. 4 (a) Reaction efficiency *vs.* time to increase the 4-NP concentration; (b) ln(A/A_0) *vs.* reaction time at different 4-NP concentrations; (c) histogram of rate constant k_{app} values; (d) reaction efficiency *vs.* time with increased $NaBH_4$ concentration; (e) ln(A/A_0) *vs.* reaction time at different $NaBH_4$ concentrations; and (f) histogram of rate constant k_{app} values.

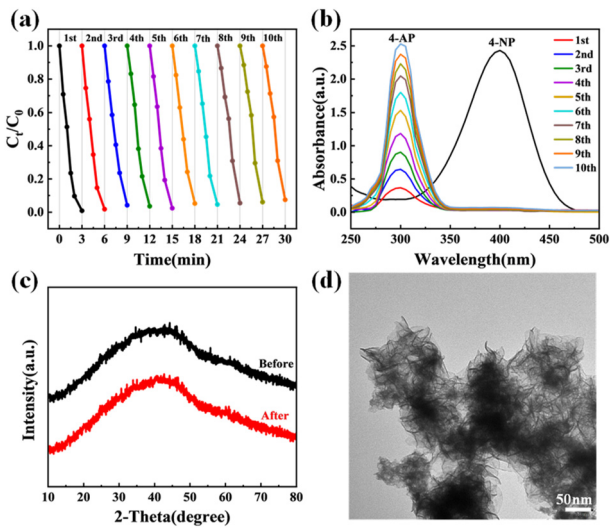

Fig. 5 (a) Reusability test of pre-prepared Ni_3Fe_1–B in 4-NP catalytic reduction at room temperature; (b) UV-visible absorption spectra of 4-AP formation; (c) XRD patterns of Ni_3Fe_1–B before and after reaction; and (d) TEM image of Ni_3Fe_1–B after reaction.

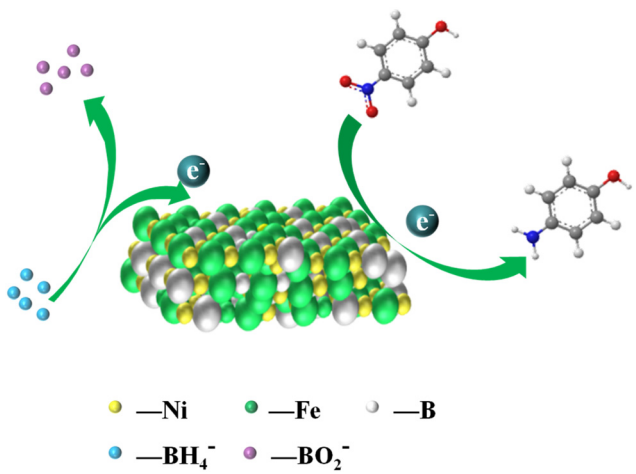

Fig. 6 Mechanistic diagram of the catalytic reduction of 4-NP.

surface, which promotes the decomposition of $NaBH_4$ and releases active hydrogen; (II) electron transfer from Ni_3Fe_1–B to adsorbed 4-NP, allowing the $-NO_2$ group to gain electrons; (III) active hydrogen generated from $NaBH_4$ is also transferred to the 4-NP molecule, reducing the $-NO_2$ group to the amino group ($-NH_2$); and (IV) desorption of product 4-AP from the catalyst surface.

The XPS analysis of Ni_3Fe_1–B before and after the reaction (Fig. S11a†) reveals that electron transfer on its surface is crucial for its catalytic activity. As shown in Fig. S11b,† the binding energy of metallic Ni decreases slightly, and the oxidation peak area reduces, indicating an increase in the electron cloud density of Ni atoms. Ni serves as an active center, becoming more reduced with a lower oxidation state. The XPS

spectrum of Fe 2p (Fig. S11c†) shows a slight decrease in the binding energy of metallic Fe and an increase in the peak area of Fe^{3+}. This suggests that Fe^{2+} readily loses electrons during the reaction, transferring them to the reactants or Ni atoms, and gets oxidized to Fe^{3+}, thereby promoting the reduction of reactants. As shown in the XPS spectra of B 1s in Fig. S11d,† the binding energy of B shifts positively by 0.4 eV after the reaction compared to before, indicating that B participates in electron transfer, altering its bonding with metal atoms and adjusting the electron cloud distribution, which increases the binding energy of M–B bonds. Ni tends to gain electrons and get reduced, Fe promotes the reduction of reactants by losing electrons, and B participates in electron transfer by adjusting its bonding with metals. The synergistic effect of the three elements achieves efficient electron transfer, driving the catalytic reaction.

As shown in Fig. S12,† the synergistic effect of Ni and Fe is demonstrated. Ni, as the main active center, adsorbs and initially activates the reactants, while Fe, after accepting electrons from Ni, experiences an increase in its electron cloud density and a change in its electronic structure. Therefore, Ni together with Fe enhances the catalyst's activity and stability. The XPS analyses of Ni–Fe–B catalysts with varying Ni/Fe metal ratios were also performed (Fig. S13†). Regulating the Ni/Fe ratio could optimize the electronic structure by modulating charge distribution between Ni (δ^-) and Fe (δ^+). A Ni-rich environment (*e.g.*, Ni_3Fe_1–B) enhances H* generation and substrate adsorption, while balanced Ni/Fe (Ni_1Fe_1–B) enables efficient electron transfer and Fe^{3+}/Fe^{2+} redox cycling for $-NO_2$ reduction. Excess Fe (Ni_1Fe_3–B) shifts the electron density to Fe, but may form passivation layers, impairing activity. Electrochemical impedance spectroscopy (EIS) demonstrates that Ni_3Fe_1–B exhibits enhanced electron transport kinetics and excellent intrinsic conductivity, as shown in Fig. S14a.† Additionally, the amorphous structure enhances the adsorption of reactants. Subsequently, cyclic voltammetry (CV) revealed that Ni_3Fe_1–B has a high specific surface area (Fig. S14b†). According to the BET data (Fig. S15†), the specific surface area of Ni_3Fe_1–B is significantly greater than those of Ni–B and Fe–B. This substantial difference has a notable impact on the catalytic reduction performance of 4-NP. The increased specific surface area of Ni_3Fe_1–B provides more active sites, enhancing the contact area between 4-NP molecules and the catalyst. Consequently, this improves the adsorption efficiency of reactant molecules on the catalyst's surface, optimizes the mass transfer efficiency in the catalytic process, accelerates the reduction rate of 4-NP, and enhances overall catalytic activity, resulting in superior performance for the catalytic reduction of 4-NP.

Conclusions

In summary, we successfully synthesized Ni–Fe–B catalysts *via* an ultrasound-assisted reduction method. Systematic investigation of Ni/Fe molar ratios (3 : 1, 1 : 1, and 1 : 3) revealed that the atomic composition critically determines both microstructure and catalytic activity. Among all tested catalysts, Ni_3Fe_1–B (Ni/Fe = 3 : 1) exhibited exceptional performance, achieving complete 4-NP conversion within 3 minutes at ambient temperature, which outperform both other bimetallic compositions (Ni_1Fe_1–B, Ni_1Fe_3–B) and monometallic counterparts (Ni–B, Fe–B). The optimized Ni_3Fe_1–B demonstrated an outstanding apparent rate constant (k_{app} = 1.363 min^{-1}), surpassing most reported non-noble metal catalysts for this transformation. This superior activity originates from: (1) optimal electronic structure modulation through boron incorporation; (2) synergistic interplay between Ni and Fe active sites; and (3) enhanced hydride transfer kinetics from $NaBH_4$. This work not only provides a new strategy for designing efficient and stable boride-based catalysts but also advances the fundamental understanding of bimetallic synergy in catalytic reduction reactions, paving the way for future developments in environmental and industrial catalysis.

Author contributions

Jianquan Wang: investigation, methodology, and writing – original draft. Fangzheng Qi: investigation. Dong Ma: methodology. Guang-Ning Liu: validation. Cuncheng Li: conceptualization, supervision, writing – review and editing, and funding acquisition.

Data availability

The data that support the findings of this study are available from the corresponding author upon reasonable request.

Conflicts of interest

There are no conflicts to declare.

Acknowledgements

This study was funded by the National Natural Science Foundation of China (Grant no. 52171179), the Collaborative Innovation Center of Yellow River Basin Pharmaceutical Green Manufacturing and Engineering Equipment, University of Jinan, Jinan 250022, P. R. China, the Jinan City University Integration Development Strategy Project (JNSX2023021), and the National Natural Science Foundation of Shandong Province (ZR2024MB006).

References

1 Z. K. Xiong, H. Zhang, W. C. Zhang, B. Lai and G. Yao, *Chem. Eng. J.*, 2019, **359**, 13–31.

2 N. K. R. Bogireddy, Y. R. Mejia, T. M. Aminabhavi, V. Barba, R. H. Becerra, A. D. A. Flores and V. Agarwal, *J. Environ. Manage.*, 2022, **316**, 115292.
3 A. R. Singh, P. S. Dhumal, M. A. Bhakare, K. D. Lokhande, M. P. Bondarde and S. Some, *Sep. Purif. Technol.*, 2022, **286**, 120380.
4 N. Dabuth, S. Thuangchon, T. Prasert, V. Yuthawong and P. Phungsai, *J. Environ. Chem. Eng.*, 2022, **10**, 107215.
5 N. Rafiei, A. Fatehizadeh, M. M. Amin, H. R. Pourzamani, A. Ebrahimi, E. Taheri and T. M. Aminabhavi, *J. Environ. Manage.*, 2021, **297**, 113349.
6 S. J. Liu, H. Wang, Z. H. Hu, X. Zhang, Y. J. Sun and F. Dong, *Proc. Natl. Acad. Sci. U. S. A.*, 2024, **121**, e2401452121.
7 W. L. Jia, F. P. Tian, M. J. Zhang, X. Y. Li, S. Ye, Y. Ma, W. Wang, Y. Zhang, C. Meng, G. Zeng and J. Liu, *J. Colloid Interface Sci.*, 2021, **594**, 254–264.
8 U. Chakraborty, G. Bhanjana, Kannu, N. Kaur, R. Sharma, G. Kaur, A. Kaushik and G. R. Chaudhary, *J. Hazard. Mater.*, 2021, **416**, 125771.
9 Q. Ding, Z. W. Kang, L. P. Cao, M. S. Lin, H. Lin and D.-P. Yang, *Appl. Surf. Sci.*, 2020, **510**, 145526.
10 P. Dong, W. J. Liu, S. J. Wang, H. L. Wang, Y. Q. Wang and C. Zhao, *Electrochim. Acta*, 2019, **308**, 54–63.
11 Y. Y. Chu, B. Y. Miao, X. Q. Zhang and R. W. Lv, *J. Water Process Eng.*, 2020, **38**, 101662.
12 Y. S. Tian, M. H. Zhou, Y. W. Pan, J. J. Cai and G. B. Ren, *Chemosphere*, 2020, **240**, 124962.
13 H. Y. Niu, Y. L. Yang, W. J. Zhao, H. Z. Lv, H. Zhang and Y. Cai, *J. Hazard. Mater.*, 2021, **401**, 123442.
14 H. J. Qin, D. Q. Yin, J. Z. Bandstra, Y. Sun, G. Cao and X. Guan, *J. Hazard. Mater.*, 2020, **383**, 121218.
15 X. Mei, J. Liu, Z. W. Guo, P. Li, S. Bi, Y. Wang, Y. Yang, W. Shen, Y. Wang, Y. Xiao, X. Yang, B. Zhou, H. Liu and S. Wu, *J. Hazard. Mater.*, 2019, **363**, 99–108.
16 P. Kulkarni, *Bioresour. Technol.*, 2013, **128**, 273–280.
17 Q. Zhou, L. Qin, Z. Y. Yin and H. Jiang, *Sep. Purif. Technol.*, 2024, **328**, 125033.
18 E. M. Abd El-Monaem, A. S. Eltaweil, G. M. El-Subruiti, M. S. Mohy-Eldin and A. M. Omer, *Environ. Sci. Pollut. Res.*, 2023, **30**, 49301–49313.
19 S. Verma, K.-H. Kim, N. Kumar, S. S. Bhattacharya, M. Naushad and R. K. Dutta, *J. Hazard. Mater.*, 2022, **429**, 128308.
20 Y. Yang, Z. Xiong, Z. Wang, Y. Liu, Z. He, A. Cao, L. Zhou, L. Zhu and S. Zhao, *J. Membr. Sci.*, 2021, **621**, 119000.
21 X. L. Pang, H. Y. Bai, H. Q. Zhao, W. Q. Fan and W. Shi, *ACS Catal.*, 2022, **12**, 1545–1557.
22 C. C. Ni, Y. F. Li, X. Z. Meng, S. L. Liu, S. Luo, J. Guan and B. Jiang, *Chem. Eng. J.*, 2021, **411**, 128485.
23 M. H. Liu, A. Q. Kong, J. L. Zhang, Y. Fu and W. Li, *Int. J. Hydrogen Energy*, 2022, **47**, 2187–2199.
24 A. Serrà, X. Alcobé, J. Sort, J. Nogués and E. Vallés, *J. Mater. Chem. A*, 2016, **4**, 15676–15687.
25 S.-C. Huang, Z.-X. You, S.-M. Jhang and C.-Y. Lin, *J. Environ. Chem. Eng.*, 2022, **10**, 108882.
26 H.-Y. Chiu, T. Wi-Afedzi, Y.-T. Liu, F. Ghanbari and K.-Y. A. Lin, *J. Water Process Eng.*, 2020, **37**, 101379.
27 H. H. Lv, M. Lin, C. Y. Yu, H. F. Wang, M. Q. Li, L. Zhang, Z. Liu and Z. Chen, *J. Environ. Chem. Eng.*, 2023, **11**, 110375.
28 N. Y. Baran, T. Baran, M. Nasrollahzadeh and R. S. Varma, *J. Organomet. Chem.*, 2019, **900**, 120916.
29 J. Li, C. Y. Liu and Y. Liu, *J. Mater. Chem.*, 2012, **22**, 8426.
30 X. Y. Qin, M. Y. Yang, P. J. Yin, X. Shi, F. Chen, Y. Gui, J. Zhao, L. Jiang and D. Luo, *Mater. Today Catal.*, 2023, **3**, 100026.
31 P. Raizada, A. Sudhaik, S. Patial, V. Hasija, A. A. P. Khan, P. Singh, S. Gautam, M. Kaur and V.-H. Nguyen, *Arabian J. Chem.*, 2020, **13**, 8424–8457.
32 Y. L. Xu, X. F. Shi, R. Hua, R. Zhang, Y. J. Yao, B. Zhao, T. Liu, J. Zheng and G. Lu, *Appl. Catal., B*, 2020, **260**, 118142.
33 X. J. Huang, D. Y. Lin, P. Duan, H. Chen, Y. Zhao, W. Yang, Q. Pan and X. Tian, *J. Colloid Interface Sci.*, 2023, **629**, 55–64.
34 S. Ye, Y. F. Wang, C. C. Wang, L. Cheng, L. Sun and P. Yan, *J. Colloid Interface Sci.*, 2023, **639**, 284–291.
35 X. Y. Qin, W. B. Lu, G. H. Chang, Y. L. Luo, A. M. Asiri, A. O. Al-Youbi and X. Sun, *Gold Bull.*, 2012, **45**, 61–67.
36 Y. Wu, X. M. Li, H. Zhao, F. B. Yao, J. Cao, Z. Chen, X. Huang, D. Wang and Q. Yang, *Chem. Eng. J.*, 2021, **418**, 129296.
37 B. W. Lu, Y. H. Wang, W. Li, S. W. Song, P. Tian, R. Li, X. Tian, X. Liu and J. Zang, *Int. J. Hydrogen Energy*, 2021, **46**, 23245–23253.
38 K. N. Dinh, Q. Liang, C.-F. Du, J. Zhao, A. I. Y. Tok, H. Mao and Q. Yan, *Nano Today*, 2019, **25**, 99–121.
39 S. Anantharaj, S. R. Ede, K. Sakthikumar, K. Karthick, S. Mishra and S. Kundu, *ACS Catal.*, 2016, **6**, 8069–8097.
40 H. R. Zhang, Q. H. Wei, G. M. Wu, S. Qiu, Y. Zou, Y. Xia, F. Xu, L. Sun and H. Chu, *J. Alloys Compd.*, 2023, **930**, 167486.
41 F. O. Baydaroglu, E. Özdemir and A. G. Gürek, *Int. J. Hydrogen Energy*, 2022, **47**, 9643–9652.
42 M. T. M. Pour and M. H. Paydar, *Int. J. Hydrogen Energy*, 2022, **47**, 36372–36380.
43 L. S. Xiao, D. Q. Jia, C. Chen, T. T. Liu, X. F. Zhang, Q. F. Huang, M. Ubaidullah, Y. Z. Sun, S. Y. Huang and Z. H. Pu, *Dalton Trans.*, 2025, **54**, 3478–3485.
44 T. T. Liu, Z. S. Chen, S. X. Liu, P. Wang, Z. H. Pu, G. X. Zhang and S. H. Sun, *Angew. Chem., Int. Ed.*, 2025, **64**, e202414021.
45 T. T. Liu, C. Chen, Z. H. Pu, Q. F. Huang, J. D. Jiang, M. Han, W. Chen, G. T. Yu, Y. Z. Sun, S. Y. Huang, Q. J. Chen, A. M. Al-Enizi, A. Nafady, X. Q. Mu and S. C. Mu, *Angew. Chem., Int. Ed.*, 2025, **64**, e202425257.
46 K. Chen, Y. Tian, Y. H. Li, Y. Liu and K. Chu, *J. Mater. Chem. A*, 2023, **11**, 7409–7414.
47 R. Li, F. M. Zhang, J. P. Zhang and H. Dong, *Int. J. Hydrogen Energy*, 2022, **47**, 5260–5268.
48 Y. Y. Xia, Y. J. Pei, Y. S. Wang, F. Li and Q. Li, *Fuel*, 2023, **331**, 125733.

49 Y. Wang, D. Wang, C. C. Zhao, W. Meng, T. Zhao, Z. Cao, K. Zhang, S. Bai and G. Li, *Int. J. Hydrogen Energy*, 2019, **44**, 10508–10518.
50 M. T. Shi, Y. J. Hou, X. H. Du, J. Guo, B. Li and Y. X. Li, *ACS Appl. Nano Mater.*, 2023, **6**, 6798–6809.
51 Y. Wang, Y. J. Tian, J. F. Zhang, C. P. Yu, R. Cai, J. Wang, Y. Zhang, J. Wu and Y. Wu, *ACS Appl. Energy Mater.*, 2020, **3**, 9516–9522.
52 Y. X. Yu, H. Liu, J. H. Zhang, H. Zhang, Y. Sun and L. C. Peng, *Renewable Energy*, 2023, **209**, 453–461.
53 Q. Q. Wang, J. Q. Li, Y. J. Li, G. M. Shao, Z. Jia and B. Shen, *Nano Res.*, 2022, **15**, 8751–8759.
54 Y. X. Yu, H. Liu, J. H. Zhang, H. Zhang, Y. Sun and L. Peng, *Renewable Energy*, 2023, **209**, 453–461.
55 Y. Q. Kang, Y. N. Guo, J. J. Zhao, B. Jiang, J. R. Guo, Y. Tang, H. Li, V. Malgras, M. A. Amin, H. Nara, Y. Sugahara, Y. Yamauchi and T. Asahi, *Small*, 2022, **18**, 2203411.
56 Z. H. Xia, L. B. Niu, Y. D. An, G. Bian, T. Li and G. Bai, *Green Chem.*, 2021, **23**, 7763–7772.
57 F. Hu, H. Y. Wang, Y. Zhang, X. C. Shen, G. H. Zhang, Y. B. Pan, J. T. Miller, K. Wang, S. L. Zhu, X. J. Yang, C. M. Wang, X. J. Wu, Y. J. Xiong and Z. M. Peng, *Small*, 2019, **15**, 1901020.
58 G. Liu, D. He, R. Yao, Y. Zhao and J. Li, *Nano Res.*, 2018, **11**, 1664–1675.
59 N. Wang, A. N. Xu, P. F. Ou, S. F. Hung, A. Ozden, Y.-R. Lu, J. Abed, Z. Wang, Y. Yan, M.-J. Sun, Y. Xia, M. Han, J. Han, K. Yao, F.-Y. Wu, P.-H. Chen, A. Vomiero, A. Seifitokaldani, X. Sun, D. Sinton, Y. Liu, E. H. Sargent and H. Liang, *Nat. Commun.*, 2021, **12**, 6089.
60 W. Z. Hong, S. F. Sun, Y. Kong, Y. Y. Hu and G. Chen, *J. Mater. Chem. A*, 2020, **8**, 7360–7367.
61 J. Strachan, C. Barnett, A. F. Masters and T. Maschmeyer, *ACS Catal.*, 2020, **10**, 5516–5521.
62 J. L. Zhu, X. Zhang, Z. H. Qin, L. X. Zhang, Y. Ye, M. Cao, L. Gao and T. Jiao, *Colloids Surf., A*, 2021, **611**, 125889.
63 J. Wang, J. Kim, J. Bu, D. Kim, S. Y. Kim, K. T. Nam, R. S. Varma, H. W. Jang, R. Luque and M. Shokouhimehr, *J. Ind. Eng. Chem.*, 2022, **107**, 428–435.
64 J. J. Yin, B. C. Ge, T. F. Jiao, Z. Qin, M. Yu, L. Zhang, Q. Zhang and Q. Peng, *Langmuir*, 2021, **37**, 1267–1278.
65 Q. Yan, X. Y. Wang, J. J. Feng, L.-P. Mei and A.-J. Wang, *J. Colloid Interface Sci.*, 2021, **582**, 701–710.
66 X. Z. Ma, J. Wen, S. Zhang, H. R. Yuan, K. Y. Li, F. Yan, X. T. Zhang and Y. J. Chen, *ACS Sustainable Chem. Eng.*, 2017, **5**, 10266–10274.
67 E. S. Melby, A. C. Mensch, S. E. Lohse, D. Hu, G. Orr, C. J. Murphy, R. J. Hamers and J. A. Pedersen, *Environ. Sci. Nano*, 2016, **3**, 45–55.